Correlation between Fermi arc and charge order resulting from the momentum-dependent self-energy correction in cuprates

Le Quy Duong*
Department of Physics, National University of Singapore, Singapore 117542

Tanmoy Das
Department of Physics, Indian Institute of Science, C. V. Raman Road, Bangalore 560012, India
(Received 6 March 2017; revised manuscript received 8 September 2017; published 27 September 2017)

We calculate momentum-dependent self-energies due to self-consistent spin and charge-density fluctuations within a single-band Hubbard model for hole-doped cuprates. We find that the dynamical density instability (mainly paramagnonlike spin fluctuations) arising from the van Hove singularity at the antinodal point produces strongly anisotropic mass renormalization, increasing from the nodal direction to the antinodal one. This gives rise to a coherent Fermi arc pattern in which although the self-energy dressed Green's function has poles at all Fermi momenta, the corresponding spectral weight decreases from the nodal to the antinodal direction. We study the feedback effects of the anisotropic self-energy and Fermi arc on the charge-density wave (CDW) instability by direct computations of charge susceptibility and the quasiparticle interference pattern. We find that that due to the loss of spectral weight at the antinodal points, the CDW nesting weakens, and the corresponding hot spot shifts from the antinodal region to the tip of the Fermi arc below the magnetic Brillouin zone. The results are in good agreement with experiments, reproducing the observed slow doping dependence of the CDW wave vector. Our investigation therefore provides a mechanism for the Fermi arc in cuprates, with various testable predictions such as a sharp, first-order-like phase transition of the CDW order on the higher-doping side.

DOI: 10.1103/PhysRevB.96.125154

I. INTRODUCTION

The mechanism of unconventional superconductivity in all material classes is often believed to be related to the origin of its exotic normal state, which is mostly non-Fermi-liquid-like and sometimes intervened by electronic and/or magnetic orders [1–6]. Cuprates are good model systems to study this problem because of their single-band electronic structure and higher superconducting (SC) transition temperature compared with other materials. Yet their normal state is extremely complicated, having a number of electronic and magnetic orders, as well as a mysterious "pseudogap" state. The pseudogap physics is often associated with the appearance of a "Fermi arc". Here, the Fermi surface (FS) loses its spectral weight as one moves from the nodal or diagonal direction to the Brillouin zone (BZ) boundary (antinodal region). Whether a broken-symmetry phase or any phase fluctuation or something else is responsible for the formation of the Fermi arc is still largely debated [7]. More recently, a similar Fermi arc feature was observed in iridium oxide (iridates) [8,9], raising the possibility that the Fermi arc could perhaps be a fundamental property of moderately or strongly correlated materials.

Recently, the charge-density wave (CDW) phase was observed in a number of hole-doped cuprates via different experimental probes [10,11]. The CDW transition temperature is often seen to be lower than the pseudogap temperature. Interestingly, the CDW wave vector was believed to arise from the nesting between the antinodal parts of the FS [12]. On the contrary, at the CDW temperature, the antinodal part is already truncated by the pseudogap, and the remaining FS gives a Fermi arc feature. More recently, combined angle-resolved photoemission spectroscopy (ARPES) and scanning tunneling microscopy (STM) measurements [via quasiparticle interference (QPI) maps] demonstrated that the CDW wave vector connects at some non-high-symmetry k points of the Fermi arc, rather than at the antinodal point in $Bi_2Sr_{2-x}La_xCuO_{6+\delta}$ (Bi2201) [11]. These observations provide a new test bed to study the mechanism of the pseudogap Fermi arc from the doping behavior of the CDW wave vector and its intensity.

In earlier model calculations by parameterizing the pseudogap as a (π,π) nesting antiferromagnetic (AF) order, it was shown that the QPI pattern obtains strong peaks at the CDW wave vector which connects the end points of the nodal FS pocket [11,13]. The extension of the AF order to the higher-doping pseudogap region is, however, not supported by experiments.

Here, we calculate the self-energy due to the density-density correlations (spin and charge densities) as a function of both momentum and frequency within a single-band Hubbard model. The computational scheme is called the momentum-resolved density fluctuation (MRDF) model as introduced previously [6,14] and successfully implemented in various correlated materials [6,14–17]. The MRDF method calculates the self-energy along the lines of fluctuation-exchange (FLEX) or GW approximations, but with the advantage that, here, both the single-particle Green's function and the two-body correlation functions are calculated self-consistently with the self-energy corrections. The Bethe-Salpeter-type vertex correction is included self-consistently and obeys Ward's identity (which means it follows the conservation laws). The calculation assumes intermediate coupling strength of the Hubbard interaction $U \sim \mathcal{W}$ (where $\mathcal{W}$ is the quasiparticle bandwidth), as appropriate for doped cuprates [6,18–22].

*Present address: Institute of Physics B5, University of Liège, B-4000 Sart-Tilman, Belgium; duong.lequyqn@gmail.com

The dominant source of the self-energy correction is the high-energy spin fluctuations lying around 200–350 meV and along the $(\pi,0)$ direction. Self-energy splits the electronic states into three energy scales [6]: there are two incoherent, localized Hubbard bands at the bottom and top of the bands at $\mathbf{k}=(0,0)$ and $\mathbf{k}=(\pi,\pi)$ and an itinerant, coherent band near the Fermi level, with a renormalized van Hove singularity (VHS) in the antinodal direction. The density fluctuations between the itinerant VHS states and the localized Hubbard states give rise to paramount spin fluctuations in the $(\pi,0)$ regions, often referred to as paramagnons. We emphasize that the self-consistency allows us to produce fluctuations between the local and itinerant electrons, and thus, the system is pushed to the intermediate-coupling regime. The corresponding self-energy therefore becomes stronger at the antinodal points and gradually decreases in the nodal region. In other words, the microscopic origin of the strong enhancement of the self-energy at the antinodal point is the positioning of the renormalized VHS in the electronic spectrum.

This characteristic self-energy behavior creates a Fermi-arc-like spectral density map at the Fermi level E_F, as directly measured by ARPES [11]. The calculation does not exhibit any broken-symmetry order parameter at finite doping. Using the same self-energy, we calculate the static charge susceptibility and the QPI maps as a function of doping. Interestingly, although the self-energy correction is dominated by the spin fluctuations, it impacts the CDW nesting via spectral weight renormalization and thereby modifies its behavior. The methodology gives a unique platform to study the evolution of the CDW wave vector in the case of a proper Fermi arc, rather than a Fermi pocket. Our result indeed shows that due to the interplay between the k-dependent spectral weight renormalization and nesting conditions, the CDW wave vector is shifted from the antinodal point, as one often suspects [12], to the tip of the Fermi arc below the magnetic zone boundary. Our results are in quantitative agreement with ARPES and QPI patterns as a function of doping. This provides a more generic and consistent description of the two complementary measurements.

The rest of the paper is arranged as follows. In Sec. II, we describe the MRDF theory, including the tight-binding model for Bi2201, density-density fluctuations, self-energy calculations, and vertex correction. In Sec. III, we present our results, where we calculate the Fermi arc feature, CDW, and QPI patterns including the k-dependent self-energy. Then we compute the QPI patterns as a function of doping and show how the CDW wave vector possesses a discontinuous jump at the critical point when the self-energy correction is included. Finally, we discuss various aspects of our methods and conclude in Sec. IV

II. MODEL: SELF-CONSISTENT SELF-ENERGY CALCULATION AND THE MRDF METHOD

We take a low-energy single-band tight-binding model fitted to the density-functional theory band structure of Bi2201 [6]. We use Bi2201 as the model system since both ARPES and STM measurements were done for the same sample. The dispersion relation can be specified as

$$\xi_{\mathbf{k}} = -2t(c_x+c_y) - 4t^{'}c_xc_y - 2t^{''}(c_{2x}+c_{2y}) \\ -4t^{'''}(c_{2x}c_y+c_xc_{2y}) - 4t^{''''}c_{2x}c_{2y} - \mu. \quad (1)$$

Here, $c_{\alpha i}=\cos\alpha k_i$, where α is a number and $i=x,y$ directions. The tight-binding parameters are $t=0.44$ eV, $t^{'}=-0.1$ eV, $t^{''}=0.057$ eV, $t^{'''}=0.005$ eV, $t^{''''}=-0.032$ eV, which is suitable for the Bi2201 system [6]. The chemical potential μ is adjusted for each doping. The presence of density-density fluctuations (mainly arising from spin and charge fluctuations) in the whole cuprate phase diagram is demonstrated by many experiments [23,24]. The density fluctuations in the intermediate-energy scales (200–350 meV) can be captured from the summation over all irreducible particle-hole bubble diagrams. This gives a random-phase approximation (RPA)-based effective correlation potential $V_\nu(\mathbf{q},\omega_p)$ ($\nu=1,2$ for spin and charge fluctuations). The feedback effect of the fluctuation potential to the electronic structure is calculated as a complex self-energy correction. The generalized form of the fully self-consistent self-energy was obtained by Hedin [25]. In our MRDF model, we calculate both the single-particle spectral function and the two-particle density-density correlation function self-consistently. We employ the Bethe-Salpeter vertex correction that preserves both the total charge and spin densities [26]. The self-consistent loop neglects the imaginary parts of the self-energy in the spectral function, which does not cause a problem since the f-sum rule is maintained by the proper choice of the vertex correction, following Ward's identity [27]. The method is described in detail in Refs. [6,14–17].

We calculate the single-band electronic self-energy due to the coupling of the density fluctuations to the electronic states within the MRDF method,

$$\Sigma_\nu(\mathbf{k},\omega) = \frac{1}{\Omega_{\mathrm{BZ}}}\sum_{\mathbf{q}}\int_{-\infty}^{\infty} d\omega_p \bar{V}_\nu(\mathbf{q},\omega_p)\Gamma_\nu(\mathbf{k},\mathbf{q},\omega,\omega_p) \\ \times\left[\frac{1-\bar{f}_{\mathbf{k}-\mathbf{q}}+n_p}{\omega+i\delta-\bar{\xi}_{\mathbf{k}-\mathbf{q}}-\omega_p}+\frac{\bar{f}_{\mathbf{k}-\mathbf{q}}+n_p}{\omega+i\delta-\bar{\xi}_{\mathbf{k}-\mathbf{q}}+\omega_p}\right]. \quad (2)$$

Here, $\mathbf{k}$ and ω are the quasiparticle momentum and frequency, and $\mathbf{q}$ and ω_p are the bosonic excitation momentum and frequency, respectively. Ω_{BZ} is the electronic phase-space volume. The quasiparticle energy is defined as $\bar{\xi}_{\mathbf{k}}=\xi_{\mathbf{k}}+\Sigma'(\mathbf{k},\bar{\xi}_{\mathbf{k}})$, where Σ' is the real part of the self-energy. We note that to keep the carrier density fixed with and without the self-energy correction, we adjust the chemical potential in both cases. $\bar{f}_{\mathbf{k}}=Z(\mathbf{k})f(\bar{\xi}_{\mathbf{k}})$ is the renormalized fermion occupation number, where the quasiparticle residue is defined as $Z_{\mathbf{k}}^{-1}=1-[\partial\Sigma'(\mathbf{k},\omega)/\partial\omega]|_{\omega=\bar{f}_{\mathbf{k}}}$. $n_p(\omega_p)$ is the boson occupation number.

$V_\nu(\mathbf{q},\omega_q)$ is the fluctuation-exchange potential generated by the spin ($\nu=1$) and charge ($\nu=2$) fluctuations: $\bar{V}_\nu(\mathbf{q},\omega_p)=(\eta_\nu/2)U^2\bar{\chi}_\nu''(\mathbf{q},\omega_p)$, where $\eta=3,1$ for spin and charge, respectively. $\bar{\chi}_\nu(\mathbf{q},\omega_p)$ is the self-energy dressed RPA correlation functions, which are related to the one-loop particle-hole polarizability $\bar{\chi}_\nu^0$ as $\bar{\chi}_\nu(\mathbf{q},\omega_p)=\bar{\chi}_\nu^0(\mathbf{q},\omega_p)/[1\mp U\bar{\chi}_\nu^0(\mathbf{q},\omega_p)]$,

where the $\mp$ sign is for spin and charge susceptibilities and U is the renormalized Hubbard interaction. The bare polarizability with the self-energy correction is defined as

$$\bar{\chi}_\nu^0(\mathbf{q},\omega_p) = \frac{1}{\Omega_{\mathrm{BZ}}} \sum_{\mathbf{k}} \frac{\Gamma_\nu(\mathbf{k},\mathbf{q},\omega_p)(\bar{f}_{\mathbf{k}} - \bar{f}_{\mathbf{k}+\mathbf{q}})}{\omega_p + i\delta - \bar{\xi}_{\mathbf{k}+\mathbf{q}} + \bar{\xi}_{\mathbf{k}}}. \quad (3)$$

In general, in a paramagnetic ground state, the bare bubble is the same for both spin and charge channels, but once self-energy is included, these two channels become decoupled since the corresponding vertex correction Γ_ν can be different for them.

Due to the momentum dependence of the self-energy, two vertex corrections arise: density vertex and current vertex. Although we are interested in only the density vertex Γ_ν, it depends on the current vertex via conservation laws. Thanks to Ward's identity, one can obtain an algebraic form of the density vertex in terms of the self-energy, $\Gamma(\mathbf{k},\mathbf{q},\omega,\omega_p) = 1 - [\partial\Sigma'(\mathbf{k}-\mathbf{q},\omega)/\partial\omega]|_{(\omega-\omega_p)} \approx Z^{-1}_{\mathbf{k}-\mathbf{q}}$, if we assume the Fermi-liquid ansatz $\Sigma' \approx (1 - Z_{\mathbf{k}}^{-1})\omega$. With this vertex correction, one can show that the band dispersion $\bar{\xi}_{\mathbf{k}}$, susceptibility $\bar{\chi}$, U, and the interaction potential $\bar{V}_\nu$ are renormalized by the same Z term, and thus, the initial intermediate-coupling theory remains valid even with the self-energy correction.

We restrict ourselves to the intermediate-coupling scenario and use $U = 2\,\mathrm{eV}$ at doping $p = 0.12$. We note that the self-energy anisotropy is not directly affected by U since the anisotropy is dictated by the position of the VHS and the localized Hubbard bands. The value of U gives only an overall amplitude shift of the self-energy. Finally, the self-energy dressed Green's function in the normal state becomes $G^{-1} = G_0^{-1} - \Sigma$, where Σ is the total self-energy and G_0 is the noninteracting Green's function. All self-energies are computed self-consistently with only the real part of the self-energy in the coherent part of the spectrum ($\leqslant$300 meV), until the total self-energy converges, as described in Refs. [6,14].

III. RESULTS

A. Momentum-dependent self-energy and mechanism of the Fermi arc

We start with the discussion of the momentum-dependent self-energy and mass renormalization. For this discussion we focus on a particular doping, $x \sim 0.12$, where CDW is dominant, so that we can build a direct link to the following CDW state later. In Fig. 1, we show the calculation of the self-energy at various representative momentum values. We observe a direct correlation between the real (Σ') and imaginary (Σ'') parts of the self-energy. As we move closer to the antinodal region, the slope of Σ' increases, and the mass renormalization $Z_{\mathbf{k}}^{-1} = [1 - \partial\Sigma'(\mathbf{k},\omega)/\partial\omega]_{\omega=0}$ is thus enhanced. Consistently, the frequency dependence of the imaginary part Σ'' also changes from $\sim \omega^2$ (Fermi-liquid-like) in the nodal region to ω in the antinodal region, which is a reflection of the marginal Fermi-liquid behavior in the region. An earlier ARPES study also found an anisotropic scattering rate (proportional to Σ''), changing from quadratic to linear energy dependence on moving from the nodal to the antinodal direction [28]. This result is in good agreement with the k-dependent behavior of our computed self-energy. However,

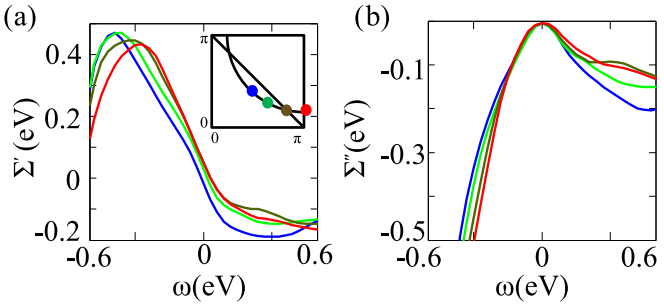

FIG. 1. Momentum-dependent self-energy for various representative momenta on the FS as indicated in the inset. (a) Real part Σ'. (b) The corresponding imaginary part Σ''. We notice that as one moves towards the antinodal point, the self-energy becomes sharper with an enhanced renormalization effect. $\Sigma'' = 0$ at $\omega = 0$ for all momenta.

$\Sigma''(\mathbf{k},0) = 0$ for all momenta. This is expected since the self-energy comes from the particle-hole continuum. Therefore, it does not contribute to the spectral weight modulation at the Fermi level; in other words, Σ'' does not produce the Fermi arc, and it comes solely from the momentum-dependent spectral weight renormalization $Z_{\mathbf{k}}$.

In Fig. 2(a), we present the full momentum-dependent mass renormalization $m^*/m_b(\mathbf{k}) = 1/Z_{\mathbf{k}}$, where m_b is the noninter-

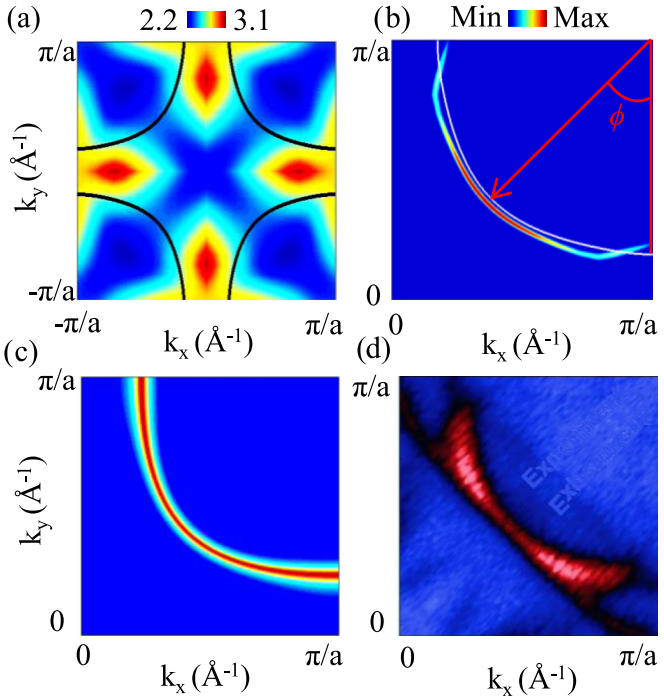

FIG. 2. (a) $\mathbf{k}$-resolved mass renormalization at the Fermi level at underdoping $p = 0.12$. The black solid line gives the corresponding noninteracting FS. (b) The spectral weight map in the first quadrant of the BZ with momentum-dependent self-energy. The white line is the corresponding noninteracting FS. ϕ is the FS angle with respect to the zone boundary. The black line in (a) and the white line in (b) are the same noninteracting band. (c) Calculated spectral weight map at E_F for the momentum-independent self-energy correction. (d) Experimental FS at the same doping level for Bi2201 (from Ref. [11]) symmetrized with respect to the zone diagonal direction.

acting band mass. The black solid line gives the noninteracting FS, which provides a reference to the k-dependent m^*/m_b values. As mentioned earlier, the strongest contribution to the renormalization comes from the spin fluctuations between the VHS region $(\pi,0)$ and the top of the band lying at (π,π). We note that once the self-energy correction is self-consistently included, it creates incoherent and localized states at the bottom and top of the bands which are reminiscent of the upper (UHB) and lower (LHB) Hubbard bands. The low-energy VHS states near the Fermi level remain coherent and itinerant [6,17]. As a result, the self-energy dressed spin fluctuation with which we are concerned is the fluctuation between the itinerant (at VHS) and localized [at the UHB at (π,π)] states. These fluctuations at the VHS are observed by resonant-inelastic x-ray scattering spectroscopy (RIXS) [6]. This is the reason why the renormalization is strongest along the antinodal region and then gradually decreases towards the nodal direction. The momentum profile of m^*/m_b is similar in all cuprates, except that the exact location of its maximum varies slightly between different materials, which is related to the shape of the VHS and the doping concentration.

1. Coherent Fermi arc

Next, we return to the discussion of how the momentum profile of $Z_{\mathbf{k}}$ gives a coherent Fermi arc. The low-energy expansion of the self-energy with respect to the Fermi energy gives $\Sigma'(\mathbf{k},\omega) \approx \Sigma'(\mathbf{k},0) + (1 - Z_{\mathbf{k}}^{-1})\omega$. Substituting this low-energy self-energy and ignoring its imaginary part Σ'' near the Fermi level, we can write the spectral function as

$$A(\mathbf{k},\omega) = \frac{1}{\pi} \frac{-Z_{\mathbf{k}}}{\{\omega - Z_{\mathbf{k}}[\xi_{\mathbf{k}} + \Sigma'(\mathbf{k},0)]\}^2 + \delta_{\mathbf{k}}^2}. \quad (4)$$

Due to the momentum-dependent self-energy, δ acquires a small momentum dependence as $\delta_{\mathbf{k}} = Z_{\mathbf{k}}\delta$. It is, however, important to notice that $\Sigma'(\mathbf{k},0)$ gives an effective anisotropic chemical potential shift to the band structure. The chemical potential μ is recalculated with self-energy to conserve the particle number. The calculated renormalization value (averaged over the BZ) comes out to be 0.4, which agrees well with experiments [29]. We emphasize that despite strong spectral weight renormalizations across the Brillouin zone, the spectral function has a well-defined pole at each Fermi momentum, defined by $\bar{\xi}_{\mathbf{k}} = Z_{\mathbf{k}}[\xi_{\mathbf{k}} + \Sigma'(\mathbf{k},0)] = 0$. Again, since our calculation yields $\Sigma''(\mathbf{k}_F) = 0$, the FS consists of long-lived quasiparticles despite the $\mathbf{k}$-dependent spectral weight renormalization, and thus, we distinguish it as a *coherent* Fermi arc.

The full self-energy dressed spectral weight map is shown in Fig. 2(b) at $\omega = 0$ and compared with the corresponding experimental data [11] in Fig. 2(d). Expectedly, the spectral weight renormalization reproduces the Fermi arc. Moreover, the shape of the Fermi arc characteristically deviates from that of the noninteracting FS [shown by the white line in Fig. 2(b)]. Along the nodal direction, the Fermi momenta are shifted inwards, while along the antinodal direction, they shift outwards. Interestingly, two earlier independent studies predicted that a single band fitting to the Fermi arc gives a larger FS area than the doping [30,31]. Our results are also qualitatively consistent with cluster dynamical mean-field theory (DMFT) [32] as well as cluster quantum Monte Carlo calculations [21]. We note that in an earlier FLEX calculation with momentum-dependent self-energy [33], the authors found that the self-energy is stronger at the magnetic hot-spot region, where the FS cuts the magnetic zone boundary. In that calculation, the dominant source of self-energy comes from the AF fluctuations at $\mathbf{Q} = (\pi,\pi)$, and the calculation did not incorporate the itinerant-localized spin fluctuation at the VHS. In our self-consistent scheme, we find the latter is dominant and thus has a dominant self-energy effect at the antinodal region and produces the Fermi arc.

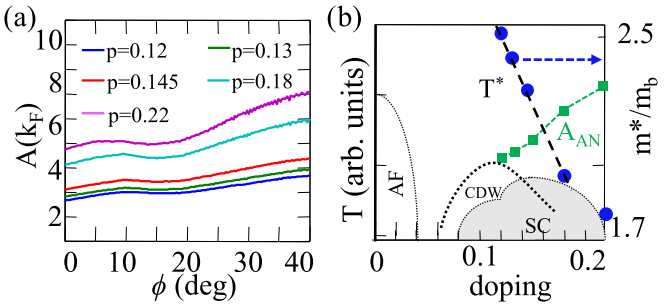

FIG. 3. (a) The spectral weight maximum is plotted as a function of FS angle ϕ for different dopings. (b) A typical phase diagram of cuprates, considering the AF and SC orders. The green squares represent doping-dependent spectral weight at the antinodal direction, and the blue circles give the mass renormalization at the same Fermi momentum. The inverse of the spectral function and the corresponding effective mass mimic the same doping dependence of the pseudogap temperature T^*.

2. Doping-dependent Fermi arc and its connection to the pseudogap physics

Next, we discuss the doping dependence of the spectral weight modulation for the same cuprate material in Fig. 3(a). As predicted in earlier calculations, the spectral weight transfer, gap collapse phenomena, and other features of the cuprate phase diagram can be quantitatively described with doping-dependent U [6,34]. We take the same strategy here. The values of U decrease almost linearly with doping; that is, when doping increases from $p = 0.12$ to $p = 0.22$, the Coulomb interaction decreases from $U = 2.0$ to $U = 1.4$ eV.

We plot $A_{\mathbf{k}_F}$ as a function of FS angle $\phi = \tan^{-1}(k_y/k_x)$ at various dopings in Fig. 3(a). We observe that the spectral weight is generally lower at the antinodal point ($\phi = 0$), compared to its value at the nodal point. The angle dependence is fairly monotonic, expect for a slight dip in $A(\mathbf{k}_F)$ near the magnetic zone boundary, which is due to the presence of low-energy AF fluctuations in the region. The overall spectral weight increases with doping, consistent with many experiments [35], due to the combined effect of the VHS moving towards the Fermi level and the Hubbard U decreasing with doping.

While the spectral weight modulation and Fermi arc are reproduced in the momentum space, the angle-integrated density of states (DOS) does not exhibit any dip in the Fermi level (not shown). This means that we have a pseudogap in the momentum-space spectral function but not in the

angle-integrated DOS. We compare the spectral weight and the mass renormalization at the antinodal point as a measure of the strength of the pseudogap at a given doping. We plot $A(\mathbf{k}_F,0)$ and the effective-mass angle-integrated m^*/m_b at $\mathbf{k}=(\pi,0)$ as a function of doping in Fig. 3(b) and compare them with the general phase diagram of Bi2201. We observe that m^*/m_b mimics the doping dependence of the pseudogap temperature. The temperature dependence is, however, not calculated in this work.

B. CDW

Based on the above-discussed spectral weight properties, we now demonstrate how the nesting condition changes with the inclusion of the momentum-dependent self-energy correction. Traditionally, CDW is assumed to arise from the antinodal nesting in cuprates [12]. But this condition is modified since the spectral weight is suppressed in the antinodal point. We evaluate the bare (one-loop) susceptibility as $\chi^0(\mathbf{q},i\omega_p)=\frac{1}{\beta\Omega_{\rm BZ}}\sum_{\mathbf{k},n}\Gamma(\mathbf{k},\mathbf{q})G(\mathbf{k},i\omega_n)G(\mathbf{k}+\mathbf{k},i\omega_n+i\omega_p)$, where G is the full self-energy dressed Green's function and ω_n and ω_p are the fermionic and bosonic Matsubara frequencies. Using the spectral representation of the Green's function, we can evaluate the fermionic Matsubara frequency summation and take the analytical continuity of the bosonic frequency $i\omega_p\rightarrow\omega_p+i\delta$. Hence, we get

$$\chi^0(\mathbf{q},\omega_p)=\frac{1}{\Omega_{\rm BZ}}\sum_{\mathbf{k}}\int_{-\infty}^{\infty}d\omega_1\int_{-\infty}^{\infty}d\omega_2\Gamma(\mathbf{k},\mathbf{q})A(\mathbf{k},\omega_1)\times A(\mathbf{k}+\mathbf{q},\omega_2+\omega_p)\frac{f(\omega_1)-f(\omega_2)}{\omega_p+i\delta-\omega_2+\omega_1}. \quad (5)$$

Here, the spectral weight is defined as $A(\mathbf{k},\omega)=-{\rm Im}G(\mathbf{k},\omega)/\pi$. [By substituting the renormalized band $\bar{\xi}_{\mathbf{k}}$ without the imaginary part of the self-energy, we can recover the bare bubble given in Eq. (3).] We compare the results of bare-bubble susceptibility and full self-energy dressed susceptibility in Figs. 4(c) and 4(d) and find characteristic differences.

The susceptibility shows three characteristic peaks: a strong peak at the AF wave vector at $\mathbf{Q}=(\pi,\pi)$, another at a stripe wave vector $\mathbf{q}\sim(\pi/4,\pi/4)$, and a third at the CDW wave vector $\mathbf{q}\sim(\pi/4,0),(0,\pi/4)$. The AF nesting comes from the nesting at the magnetic hot spot, while the latter two come from the antinodal region. Due to the spectral weight loss at the antinodal point [Fig. 4(a)], the CDW nesting strength is also substantially reduced. This can be concluded by comparing the susceptibility without and with self-energy correction in Figs. 4(c) and 4(d). Moreover, the CDW hot spot is also shifted from the antinodal region to somewhere below the magnetic zone, as shown by the arrow in Fig. 4(b).

C. QPI

We can visualize the same CDW nesting vector from the QPI pattern. Unlike the many-body interaction, the impurity scattering is dominantly elastic (assuming a large impurity potential). We calculate the QPI pattern within a single scalar impurity approximation as [36]

$$B(\mathbf{q},i\omega_n)=\frac{1}{\Omega_{\rm BZ}}V_{\rm imp}\sum_{\mathbf{k}}{\rm Im}[G(\mathbf{k},i\omega_n)G(\mathbf{k}+\mathbf{q},i\omega_n)], \quad (6)$$

where $V_{\rm imp}$ is the impurity potential, which is set to 1 here. Due to elastic scattering, we can simply take the analytical continuation of the Matsubara frequency $i\omega_n\rightarrow\omega+i\delta$ on both sides. The momentum summation is performed over the full BZ, but without imposing the reciprocal lattice boundary conditions, which helps us present the scattering vectors $|\mathbf{q}|>\pi$ explicitly, as done in experimental Fourier transformations.

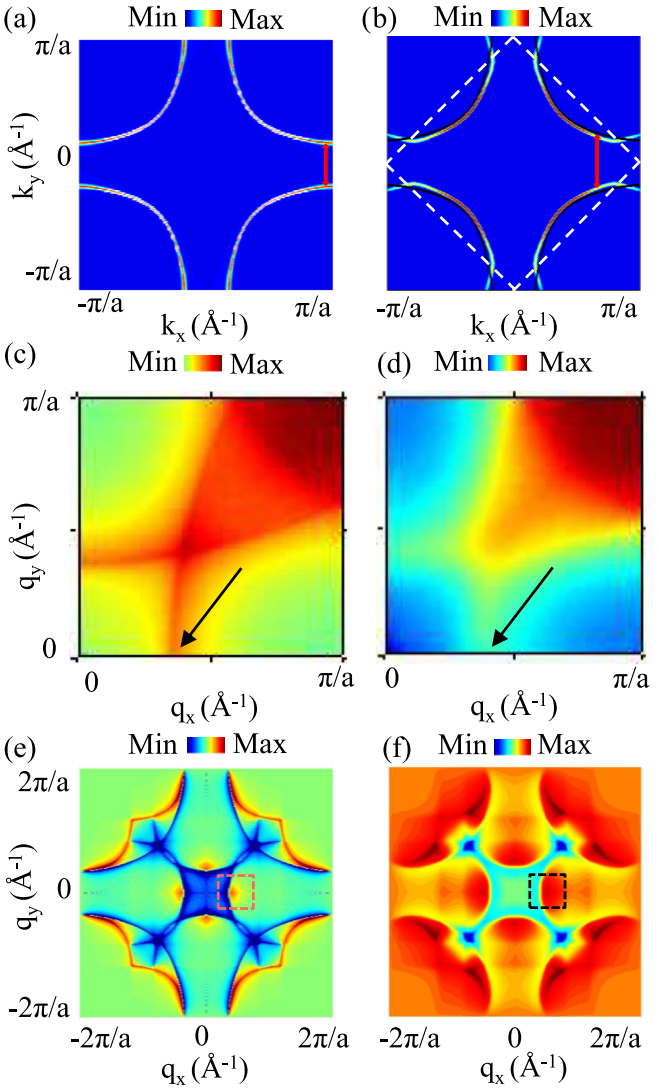

FIG. 4. Full k-dependent spectral weight maps at the Fermi level for $p=0.12$ (a) without and (b) with self-energy corrections. Dashed lines depict the magnetic zone boundary. The arrows indicate the corresponding CDW hot spots. Static charge susceptibility (c) without and (c) with self-energy correction. The arrows indicate the CDW wave vector, which is increased in the case of the self-energy correction, while the intensity is substantially decreased due to the Fermi arc. (e) and (f) Corresponding QPI maps at $\omega=0$. Tiny squares highlight the location of the CDW wave vectors.

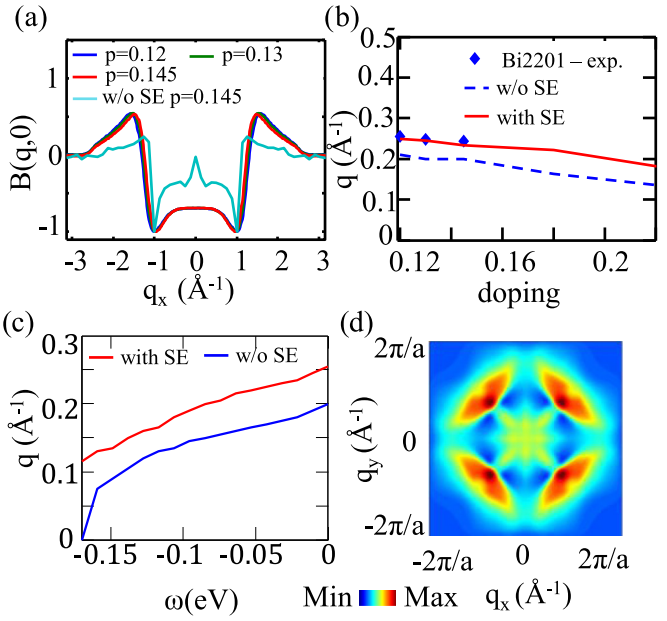

FIG. 5. (a) QPI profile along the $q_y = 0$ cut for different dopings. (b) CDW vector as a function of doping without (solid line) and with (dashed line) self-energy correction, compared with corresponding experimental data (symbols) for three doping levels, $p = 0.12$, 0.13, and 0.145, from Ref. [11]. (c) CDW q vector as a function of ω. (d) QPI pattern with self-energy at $\omega = -0.17$ eV, near the VHS of the noninteracting band for $p = 0.12$.

We calculate the QPI profiles at $\omega = 0$ in the normal state by using Eq. (6), and the results are shown in Fig. 4 for $p = 0.12$ [37]. We focus here on the CDW scattering vector along $\mathbf{q} \to (\pi,0)$ and its equivalent directions, as highlighted in Figs. 4(e) and 4(f). The QPI map without self-energy correction is shown in Fig. 4(f). Here, the corresponding CDW wave vector arises from the FS nesting at the antinodal region, as shown by the arrow in the corresponding spectral weight map in Fig. 4(a). As the k-dependent self-energy correction is included in the calculations, the QPI peaks become broad. Note that without the momentum dependence in the self-energy, the QPI map at $\omega = 0$ should not be expected to be broader than its noninteracting counterpart, as long as $\Sigma''(k_F) = 0$. The CDW wave vector also increases here since it now arises from the enhanced scattering between some non-high-symmetry points on the Fermi arc (indicated by an arrow). It is also interesting to note that the Fermi momenta corresponding to the CDW wave vector do not exactly correspond to the magnetic BZ boundary, as proposed earlier in the AF pseudogap model [11], but below the magnetic BZ at the tip of the Fermi arc.

D. First-order-like CDW phase transition with doping

Figure 5(a) gives the QPI values along the $q_y = 0$ direction for different doping concentrations. Interestingly, at the CDW wave vector, we see that the QPI value $B(q,0)$ not only shows a peak but then sharply drops and becomes negative. Without the self-energy correction, the peak on the positive side is fairly weak, whereas a clear peak develops as the self-energy correction is included. Considerably weak doping dependence of the CDW wave vector occurs with self-energy correction, compared to its noninteracting value, as shown in Fig. 5(b). These results are in good agreement with experimental data (shown by diamonds) [11]. The CDW wave vector decreases smoothly with doping with and without self-energy correction. Without self-energy correction, the CDW wave vector extrapolates to zero at the doping where the VHS reaches the Fermi level. On the contrary, it should vanish to zero discontinuously with self-energy corrections. This is because, in the latter case, the scattering hot spot lies away from the antinodal region. Therefore, even when the VHS reaches the Fermi level, where the antinodal Fermi momentum just approaches $\mathbf{k} = (\pi,0)$, the CDW hot spot still lies below the antinodal point, and the corresponding scattering wave vector remains finite. Above this doping, the FS topology changes to electronlike, and the pseudogap and the CDW wave vector both vanish. This result implies that within the present model, the CDW phase transition as a function of doping is first order. This result is demonstrated in Fig. 5(c), which shows the CDW wave vector as a function of ω until the VHS point for the noninteracting band when $\mathbf{q} \to 0$. However, with self-energy correction, the $\mathbf{q}$ vector is still finite. Figure 5(d) shows that the QPI pattern dressed by self-energy at $\omega = -0.17$ eV (where the VHS is approaching ω) is very different than the case with $\omega = 0$ presented in Fig. 4(f). Notably, recent transport measurements exhibited the existence of a sharp, first-order-like phase transition of the pseudogap phenomena around the optimal doping in $YBa_2Cu_3O_{7-\delta}$ (YBCO) [38] and in $La_{(1.6-x)}Nd_{0.4}Sr_xCuO_4$ (Nd-LSCO) [39], which is similar to what we predict in Fig. 5(c).

IV. DISCUSSION AND CONCLUSION

Here, we highlight some of the aspects of the MRDF model and the results.

(i) The MRDF method is very similar to Hedin's equations for self-energy calculation using density-density fluctuations [25]. Different approximations are usually distinguished by different models, such as FLEX [40] and GW methods [41,42]. In the FLEX approach [40], one calculates the single-particle Green's function self-consistently but not the two-particle one. However, in the GW approach, one often neglects the vertex correction or uses a quasiparticle-GW approximation [42]. In our approach, we have calculated both the single-particle Green's function and the density-density correlation function by including the self-energy correction. A Bethe-Salpeter vertex correction is included within Ward's identity to maintain the f-sum rules [26].

The self-energy calculation often suggests a perturbative treatment of the interaction terms. The method is valid up to the intermediate-coupling regime, where the correlation energy is of the order of the kinetic energy. There is an increasing consensus that cuprates lie in the intermediate-coupling regime, at least in the finite-doping range. We have shown that the intermediate-coupling range remains intact even with the self-energy correction in the fluctuation-exchange potential V. As we discussed in Sec. II, this is ensured by the vertex correction. With the Ward identity being taken into account, we observed that both the kinetic energy $\bar{\xi}_{\mathbf{k}}$ and the potential energy $\bar{V}$ are renormalized by the same renormalization factor Z, ensuring their ratio is $\mathcal{W}/U \gtrsim 1$. This ensures that the

method maintains the intermediate coupling strength and also follows the f-sum rule, an important internal check for the self-energy calculations.

(ii) Momentum-dependent self-energy was calculated earlier with a variety of methods. Usually, with cluster DMFT and dynamical cluster approximation [43], the momentum-dependent calculation is done in small clusters, and the results are in general agreement with ours. FLEX and GW methods, which can retain the full spectrum of the correlation potential, can account for the full momentum dependence of the self-energy [15,17,33,44]. In an earlier FLEX calculation [33], it was found that the self-energy effect is maximum at the AF hot spot, rather than at the antinodal points. The apparent discrepancy between the FLEX method and our MRDF method arises from how the spin-fluctuation potential is treated. Spin fluctuation have multiple high-intensity regions. At the AF wave vector $\mathbf{Q} = (\pi,\pi)$, magnon modes appear in the very low energy region ($\sim$70 meV) due to the nesting across the AF hot spot. The AF fluctuation usually dies off faster with doping in cuprates and does not contribute much beyond $x >$ 5%–7% doping [3]. Here, the dominant self-energy correction comes from the high-energy spin fluctuations, or paramagnons, which arise from the fluctuation between the itinerant and localized densities. These fluctuations lie in the antinodal region and dominate at the optimal dopings where the VHS reaches the Fermi level. The present self-energy mainly stems from the VHS fluctuations and therefore causes the Fermi arc. The Fermi arc arises solely from the momentum-dependent mass renormalization $Z_{\mathbf{k}}$ since the imaginary part Σ'' is zero at $\omega = 0$ at all momenta. This means, even in the Fermi arc, there is a well-defined pole at all momenta, but the spectral weight is modulated by $Z_{\mathbf{k}}$. The lost spectral weight in the antinodal region is transferred to the high-energy Hubbard bands via the above-mentioned spin-fluctuation channels. The frequency-dependent DOS shows three characteristic peaks: LHBs and UHBs just outside the noninteracting band edges and a coherent, itinerant peak at the VHS. The self-energy is analytic at all momenta and frequencies, and the coherent Fermi arc feature does not show up as any dip in the DOS at the Fermi level.

(iii) As noted in Sec. III, the Fermi arc feature gradually disappears near the optimal doping. However, as the CDW arises from the nesting below the magnetic zone boundary, the corresponding CDW wave vector remains finite (see Fig. 5) and sharply drops to zero as the VHS crosses above the Fermi level. This apparently drives a first-order-like discontinuous phase transition of the CDW state, as also seen in YBCO [38] and in Nd-LSCO [39]. This result is in sharp contrast to the usual hot-spot scenario, in which the hole pocket ends at the magnetic zone boundary. We find that the CDW hot spot is also not at the AF zone boundary, in contrast to the AF model of the hole-pocket scenario.

The pseudogap feature, however, smoothly vanishes when the VHS crosses the Fermi level upon doping, which is seemingly consistent with some existing experimental data for different cuprate compounds [45,46]. As temperature increases, we expect that no sharp phase transition will occur for the pseudogap state, and only the spectral weight is gradually transferred from the nodal region to the antinodal one. Consistently, the strange metal phase of the hole-doped cuprates at the optimal doping, without a phase transition, is also presented in a large number of measurements [3].

ACKNOWLEDGMENTS

L.Q.D. gratefully acknowledges Y. P. Feng and H. Lin for mentorship and the freedom to pursue this project. We thank W.-F. Tsai for critical reading of the manuscript. T.D. acknowledges the financial support from the Department of Science and Technology (DST) under the Start Up Research Grant (Young Scientist) (SERB No. YSS/2015/001286]).

[1] E. Fradkin, S. A. Kivelson, and J. M. Tranquada, Rev. Mod. Phys. **87**, 457 (2015).
[2] J. C. Davis and D.-H. Lee, Proc. Natl. Acad. Sci. USA **110**, 17623 (2013).
[3] T. Das and C. Panagopoulos, New J. Phys. **18**, 103033 (2016).
[4] B. Keimer, S. A. Kivelson, M. R. Norman, S. Uchida, and J. Zaanen, Nature (London) **518**, 179 (2015).
[5] L. Taillefer, Annu. Rev. Condens. Matter Phys. **1**, 51 (2010).
[6] T. Das, R. S. Markiewicz, and A. Bansil, Adv. Phys. **63**, 151 (2014).
[7] T. Yoshida, M. Hashimoto, I. M. Vishik, Z.-X. Shen, and A. Fujimori, J. Phys. Soc. Jpn. **81**, 011006 (2012); A. Kaminski, T. Kondo, T. Takeuchi, and G. Gu, Philos. Mag. **95**, 453 (2015).
[8] Y. K. Kim, O. Krupin, J. D. Denlinger, A. Bostwick, E. Rotenberg, Q. Zhao, J. F. Mitchell, J. W. Allen, and B. J. Kim, Science **345**, 187 (2014).
[9] G. Affeldt, T. Hogan, C. L. Smallwood, T. Das, J. D. Denlinger, S. D. Wilson, A. Vishwanath, and A. Lanzara, Phys. Rev. B **95**, 235151 (2017).
[10] G. Ghiringhelli, M. Le Tacon, M. Minola, S. Blanco-Canosa, C. Mazzoli, N. B. Brookes, G. M. De Luca, A. Frano, D. G. Hawthorn, F. He, T. Loew, M. M. Sala, D. C. Peets, M. Salluzzo, E. Schierle, R. Sutarto, G. A. Sawatzky, E. Weschke, B. Keimer, and L. Braicovich, Science **337**, 821 (2012)
[11] R. Comin, A. Frano, M. M. Yee, Y. Yoshida, H. Eisaki, E. Schierle, E. Weschke, R. Sutarto, F. He, A. Soumyanarayanan, Y. He, M. Le Tacon, I. S. Elfimov, J. E. Hoffman, G. A. Sawatzky, B. Keimer, and A. Damascelli, Science **343**, 390 (2014)
[12] S. E. Sebastian, N. Harrison, and G. G. Lonzarich, Rep. Prog. Phys. **75**, 102501 (2012).
[13] T. Das, R. S. Markiewicz, and A. Bansil, Phys. Rev. B **77**, 134516 (2008).
[14] T. Das and K. Dolui, Phys. Rev. B **91**, 094510 (2015).
[15] R. S. Dhaka, T. Das, N. C. Plumb, Z. Ristic, W. Kong, C. E. Matt, N. Xu, K. Dolui, E. Razzoli, M. Medarde, L. Patthey, M. Shi, M. Radovic, and J. Mesot, Phys. Rev. B **92**, 035127 (2015).

[16] T. Das, J.-X. Zhu, and M. J. Graf, Phys. Rev. Lett. **108**, 017001 (2012); T. Das, T. Durakiewicz, J.-X. Zhu, J. J. Joyce, J. L. Sarrao, and M. J. Graf, Phys. Rev. X **2**, 041012 (2012).
[17] X. Yin, S. Zeng, T. Das, G. Baskaran, T. C. Asmara, I. Santoso, X. Yu, C. Diao, P. Yang, M. B. H. Breese, T. Venkatesan, H. Lin, Ariando, and A. Rusydi, Phys. Rev. Lett. **116**, 197002 (2016).
[18] R. Preuss, W. Hanke, C. Gröber, and H. G. Evertz, Phys. Rev. Lett. **79**, 1122 (1997).
[19] A. Comanac, L. de' Medici, M. Capone, and A. J. Millis, Nat. Phys. **4**, 287 (2008).
[20] R. S. Markiewicz, T. Das, S. Basak, and A. Bansil, J. Electron Spectrosc. Relat. Phenom. **181**, 23 (2010).
[21] A. Macridin, M. Jarrell, T. Maier, and D. J. Scalapino, Phys. Rev. Lett. **99**, 237001 (2007).
[22] C. Weber, K. Haule, and G. Kotliar, Nat. Phys. **6**, 574 (2010).
[23] B. Vignolle, S. M. Hayden, D. F. McMorrow, H. M. Rnnow, B. Lake, C. D. Frost, and T. G. Perring, Nat. Phys. **3**, 163 (2007).
[24] J. M. Tranquada, H. Woo, T. G. Perring, H. Goka, G. D. Gu, G. Xu, M. Fujita, and K. Yamada, Nature (London) **429**, 534 (2004).
[25] L. Hedin, Phys. Rev. **139**, A796 (1965); L. Hedin and S. Lundqvist, in *Solid State Physics*, edited by F. Seitz, H. Ehrenreich, F. Seitz, and D. Turnbull (Academic, New York, 1969), Vol. 23, p. 1.
[26] E. E. Salpeter and H. A. Bethe, Phys. Rev. **84**, 1232 (1951).
[27] J. C. Ward, Phys. Rev. **78**, 182 (1950).
[28] J. Chang, M. Mansson, S. Pailhès, T. Claesson, O. J. Lipscombe, S. M. Hayden, L. Patthey, O. Tjernberg, and J. Mesot, Nat. Commun. **4**, 2559 (2013).
[29] N. P. Armitage, F. Ronning, D. H. Lu, C. Kim, A. Damascelli, K. M. Shen, D. L. Feng, H. Eisaki, Z.-X. Shen, P. K. Mang, N. Kaneko, M. Greven, Y. Onose, Y. Taguchi, and Y. Tokura, Phys. Rev. Lett. **88**, 257001 (2002).
[30] K. B. Dave, P. W. Phillips, and C. L. Kane, Phys. Rev. Lett. **110**, 090403 (2013).
[31] L. P. Gor'kov and G. B. Teitel'baum, arXiv:cond-mat/0607010.
[32] S. S. Kancharla, B. Kyung, D. Senechal, M. Civelli, M. Capone, G. Kotliar, and A.-M. S. Tremblay, Phys. Rev. B **77**, 184516 (2008).
[33] H. Kontani, K. Kanki, and K. Ueda, Phys. Rev. B **59**, 14723 (1999); H. Kontani, Rep. Prog. Phys. **71**, 026501 (2008).
[34] C. Kusko, R. S. Markiewicz, M. Lindroos, and A. Bansil, Phys. Rev. B **66**, 140513(R) (2002).
[35] R. S. Markiewicz, T. Das, and A. Bansil, Phys. Rev. B **82**, 224501 (2010).
[36] T. Das, R. S. Markiewicz, A. Bansil, and A. V. Balatsky, Phys. Rev. B **85**, 224535 (2012); A. V. Balatsky, I. Vekhter, and J.-X. Zhu, Rev. Mod. Phys. **78**, 373 (2006).
[37] Experimental QPI profiles are often calculated by convoluting the local density of states and are thus always positive. In theory, the elastic scattering process involves convolution between the complex Green's functions and thus can obtain both positive and negative signs.
[38] O. Cyr-Choinière, R. Daou, F. Laliberté, C. Collignon, S. Badoux, D. LeBoeuf, J. Chang, B. J. Ramshaw, D. A. Bonn, W. N. Hardy, R. Liang, J.-Q. Yan, J.-G. Cheng, J.-S. Zhou, J. B. Goodenough, S. Pyon, T. Takayama, H. Takagi, N. Doiron-Leyraud, and L. Taillefer, arXiv:1703.06927.
[39] C. Collignon, S. Badoux, S. A. A. Afshar, B. Michon, F. Laliberté, O. Cyr-Choinière, J.-S. Zhou, S. Licciardello, S. Wiedmann, N. Doiron-Leyraud, and L. Taillefer, Phys. Rev. B **95**, 224517 (2017).
[40] G. Baym and L. P. Kadanoff, Phys. Rev. **124**, 287 (1961); G. Baym, *ibid.* **127**, 1391 (1962).
[41] F. Aryasetiawan and O. Gunnarsson, Rep. Prog. Phys. **61**, 237 (1998); W. G. Aulbur, L. Jonsson, and J. W. Wilkins, *In Solid State Physics*, edited by H. Ehrenreich and F. Spaepen (Academic, New York, 2000), Vol. 54, p. 1.
[42] Y. Takada, Phys. Rev. Lett. **87**, 226402 (2001); S. V. Faleev, M. van Schilfgaarde, and T. Kotani, *ibid.* **93**, 126406 (2004); T. Das, R. S. Markiewicz, and A. Bansil, Europhys. Lett. **96**, 27004 (2011).
[43] Th. Maier, M. Jarrell, Th. Pruschke, and J. Keller, Eur. Phys. J. B **13**, 613 (2000).
[44] T. Miyake, C. Martins, R. Sakuma, and F. Aryasetiawan, Phys. Rev. B **87**, 115110 (2013).
[45] S. Benhabib, A. Sacuto, M. Civelli, I. Paul, M. Cazayous, Y. Gallais, M.-A. Méasson, R. D. Zhong, J. Schneeloch, G. D. Gu, D. Colson, and A. Forget, Phys. Rev. Lett. **114**, 147001 (2015).
[46] R. S. Markiewicz, J. Phys. Chem. Solids **58**, 1179 (1997); R. S. Markiewicz, I. G. Buda, P. Mistark, and A. Bansil, arXiv:1505.04770.